



Cite this: *Mol. Syst. Des. Eng.*, 2018, 3, 741

Modification of the fluorinated tin oxide/electron-transporting material interface by a strong reductant and its effect on perovskite solar cell efficiency†

Federico Pulvirenti,^a Berthold Wegner,^{bc} Nakita K. Noel,^d Giulio Mazzotta,^d Rebecca Hill,^a Jay B. Patel,^d Laura M. Herz,^d Michael B. Johnston,^d Moritz K. Riede,^d Henry J. Snaith,^d Norbert Koch,^{bc} Stephen Barlow^a and Seth R. Marder^{id}*^a

To date, the most efficient hybrid metal halide perovskite solar cells employ TiO₂ as electron-transporting material (ETM), making these devices unstable under UV light exposure. Replacing TiO₂ with fullerene derivatives has been shown to result in improved electronic contact and increased device lifetime, making it of interest to assess whether similar improvements can be achieved by using other organic semiconductors as ETMs. In this work, we investigate perylene-3,4:9,10-tetracarboxylic bis(benzimidazole) as a vacuum-processable ETM, and we minimize electron-collection losses at the electron-selective contact by depositing pentamethylcyclopentadienyl cyclopentadienyl rhodium dimer, (RhCp*₂)₂, on fluorinated tin oxide. With (RhCp*₂)₂ as an interlayer, ohmic contacts can be formed, there is interfacial doping of the ETM, and stabilized power conversion efficiencies of up to 14.2% are obtained.

Received 5th June 2018,
Accepted 1st August 2018

DOI: 10.1039/c8me00031j

rsc.li/molecular-engineering

Design, System, Application

Materials selection is essential to enable the commercialization of perovskite solar cells (PSCs). Replacing metal oxides with organic electron-transporting materials (ETMs) increases the operational stability of solar cells under UV-light exposure and provides a better electronic contact with the perovskite. However, the interface between an organic semiconductor and an electrode material can be detrimental to charge extraction if the electronic alignment is not properly adjusted. Here, we use the organometallic dimer (RhCp*₂)₂, which behaves as a masked form of the highly reducing (RhCp*₂)⁺, to investigate the impact of the electrode/ETM interface on charge collection in PSCs. (RhCp*₂)₂ not only places the electrode and the ETM in ohmic contact, but it induces interfacial doping of the ETM. Perylene-3,4:9,10-tetracarboxylic bis(benzimidazole) (PTCBI) is chosen as a vacuum-processable alternative to C₆₀ as ETM for two reasons: firstly, PTCBI and fullerenes have similar electron affinities, and secondly, perylene derivatives can be inexpensive and stable to temperature and humidity, as evidenced by finding applications in car paint. By vacuum-depositing (RhCp*₂)₂ between the electrode and PTCBI, solar cells exhibiting stabilized power conversion efficiencies up to 14.2% can be fabricated, outperforming solar cells with no organometallic dimer (12.7%).

Introduction

Metal halide perovskite solar cells (PSCs) have emerged as a promising photovoltaic technology because of their poten-

tially low manufacturing costs and their high power conversion efficiencies.¹ To date, the PSCs that can most efficiently convert sunlight to electrical energy are fabricated using TiO₂ as an electron-transporting material (ETM).² However, while these devices may be extremely efficient in the short term, it is well known that TiO₂ is unstable under UV irradiation.^{3,4} Replacing TiO₂ with molecular ETMs, such as C₆₀, has previously been shown to reduce the hysteresis present in the current-voltage (*J-V*) curves of these devices, and to increase device lifetimes under operating conditions.⁵ Fullerene-based molecules provide good electronic contact with the perovskite absorber, and do not seem to induce a high density of defects at this interface, which would otherwise cause charge recombination.^{6–9} These findings have instigated the investigation of other organic semiconductors as ETMs in PSCs.^{10–12}

^a School of Chemistry and Biochemistry and Center for Organic Photonics and Electronics (COPE), Georgia Institute of Technology GA, Atlanta 30332-0400, USA. E-mail: seth.marder@chemistry.gatech.edu

^b Institut für Physik & IRIS Adlershof, Humboldt-Universität zu Berlin, Brook-Taylor-Str. 6, D-12489 Berlin, Germany

^c Helmholtz-Zentrum Berlin für Materialien und Energie GmbH, Albert-Einstein-Str. 15, 12489 Berlin, Germany

^d Clarendon Laboratory, Department of Physics, University of Oxford, Parks Road, Oxford, OX1 3PU, UK

† Electronic supplementary information (ESI) available: Additional UPS, IPES, XPS, UV-vis-NIR, and solar cell data; discussion of XPS Rh 3d assignments. See DOI: 10.1039/c8me00031j

In particular, perylene diimides (PDIs) and related compounds are of interest because they have similar electron affinities to fullerenes, can be processed from solution or vacuum by simply tailoring their structure, and can exhibit electron mobilities of $10^{-3} \text{ cm}^2 \text{ V}^{-1} \text{ s}^{-1}$ or more.¹³ Furthermore, some perylene derivatives can be essentially insoluble, thermally resistant, and inexpensive, sufficiently so that some have been used as pigments in car paint.^{14,15} In the context of PSCs, PDIs have been used as hole-blocking layers in conjunction with fullerenes,^{16–18} as passivation layers on the surface of TiO_2 ,¹⁹ and as solution-processed electron-selective layers,²⁰ reaching power conversion efficiencies as high as 17.7%.²¹ However, “n-i-p” PSCs with thermally evaporated perylene-based ETMs still lag behind in device performance (7.9%)²² relative to their solution-processed counterparts.²¹ In the n-i-p device architecture, the ETM is deposited on top of fluorinated tin oxide (FTO), the electron-collecting electrode, and the active lead halide perovskite is then grown on the ETM, which, if the perovskite is to be solution-processed, further requires that the ETM should be insoluble in the perovskite precursor solution.

Efficient charge collection depends on the electronic energy-level alignment at the interface between the electrode and the organic semiconductor. The large energy offset between the electron affinity (EA) of the C_{60} or PDIs (3.9–4.0 eV)²³ and the work-function (WF) of the FTO (4.6 eV) is potentially detrimental to charge extraction. One potential strategy to overcoming this issue is the introduction of interlayers to adjust the energy alignment at an organic layer/electrode interface, such that the Fermi level (E_F) of the electrode is pinned to the lowest unoccupied molecular orbital (LUMO) of the organic ETM, thus minimizing losses due to inadequate electron collection.²⁴ Depending on the interlayer, the molecules of ETM near the interface can be n-doped through an electron transfer, from the electrode or from the interlayer itself, to the ETM. One approach to introducing such interlayers is to treat the electrode with a strong reductant that creates a dipole by electron transfer to the electrode.^{25,26} Dimers of nineteen-electron organometallic sandwich compounds are one class of reductants that have been used in this context, and have been shown to decrease the WF of metals and metal oxides by more than 1 eV.^{27,28} These materials have also been used as molecular n-dopants for organic semiconductors with electron affinities (EA) as low as 2.8–3.0 eV.²⁹ In both cases, these organometallic dimers react to form the corresponding monomeric cations. These dimers can be processed from both solution and vacuum, and are moderately air-stable.

In this work, we investigate how a vacuum-deposited and essentially insoluble PDI-like molecule, perylene-3,4,9,10-tetracarboxylic bis(benzimidazole) (PTCBI, Fig. 1) – the condensation product of *o*-phenylene diamine and perylene-3,4,9,10-tetracarboxylic dianhydride – compares to C_{60} (Fig. 1) as an ETM in n-i-p perovskite solar cells, along with use of one of the above mentioned dimers – pentamethylcyclopentadienyl cyclopentadienyl rhodium dimer (RhCp^*Cp)₂ (**1**₂, Fig. 1) – as

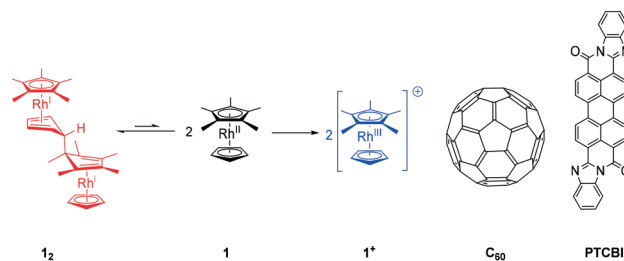


Fig. 1 Molecular structures of the neutral dimeric dopant (**1**₂), neutral monomer (**1**), cationic monomer (**1**⁺), and of the electron-transporting materials C_{60} and PTCBI.

an interlayer between FTO and PTCBI to minimize electron-collection losses at the electron-selective contact. We adopt C_{60} as a reference ETM, and correlate changes in the electronic alignment (*e.g.*, electrode WF and EA of organic semiconductor) with device performance characteristics, and demonstrate stabilized power conversion efficiencies as high as 14.2% for interface-modified PTCBI.

Experimental

Materials synthesis and purification

PTCBI (Sigma-Aldrich) was purified in three cycles *via* thermal gradient sublimation prior to loading the source material into the high vacuum deposition system.³⁰ Triple-sublimed C_{60} (purity > 99.9%, HPLC) was purchased from CreaPhys GmbH. $(\text{RhCp}^*\text{Cp})_2$ was synthesized according to literature methods.^{29,31}

Photoelectron spectroscopy

The UPS, XPS and IPES spectra were recorded in a lab system consisting of an analysis chamber (base pressure: 10^{-9} mbar) connected to a load-lock chamber (base pressure: 5×10^{-8} mbar). UPS was performed using a helium-gas-discharge lamp (21.218 eV) with low photon flux (attenuated by an aluminium filter) in order to avoid radiation damage of the samples. The secondary electron cut-off (SECO) spectra were measured with a bias of -10 V applied to the sample to clear the analyser WF. The excitation source for XPS measurements was non-monochromated Al $K\alpha$ (1486.7 eV). An Omicron EA125 hemispherical energy analyzer was used to collect the spectra in normal emission geometry (energy resolutions for UPS and XPS measurements, determined from the Au Fermi edge and the Au $4f_{7/2}$ peak, were 180 meV and 1.2 eV, respectively). The error of XPS binding energies retrieved from curve fitting is estimated to be smaller than 50 meV, as obtained from procedures where binding energies were purposely offset. IPES measurements (incident electron energy range: 5–15 eV, NaCl-coated photocathode, SrF_2 -window) were performed in the isochromat mode. All UPS, XPS and IPES spectra were recorded at room temperature.

Solar cell fabrication

Fluorinated tin oxide (FTO) coated glass sheets (Hartford Glass, $15 \Omega \square^{-1}$) were etched using a 2 M HCl solution and

zinc powder. After initial washing with Hellmanex™ III detergent, substrates were immersed for 90 min in a H₂SO₄:H₂O₂ 3:1 (v/v) piranha solution. The FTO substrates were rinsed with deionized water, and dried with compressed dry air. The substrates were deposited on a mask and loaded on a vacuum deposition chamber, where (RhCp**Cp*)₂, C₆₀ or PTCBI were sequentially deposited at 10⁻⁶ mbar at a rate of 0.1 Å s⁻¹. The samples were transferred to a different vacuum chamber for the co-evaporation of PbI₂ and CH₃NH₃I at 10⁻⁶ mbar. Alternatively, a CH₃NH₃PbI₃ solution was prepared by bubbling dry methylamine gas into a black dispersion of perovskite precursors (1.00 CH₃NH₃I:1.06 PbI₂) in acetonitrile at a concentration of 0.5 M, until the dispersion turned into a clear, light yellow solution as described in the literature.³² The resulting CH₃NH₃PbI₃ solution in acetonitrile/methylamine was spin-coated onto the substrate at 2000 rpm for 45 s in a nitrogen-filled glovebox. The dense perovskite layers obtained from spin-coating were annealed at 100 °C for 60 min. After the substrates were cooled down to room temperature, the hole-transporting material 2,2',7,7'-tetrakis(*N,N'*-di-*p*-methoxyphenylamine)-9,9'-spirobifluorene (spiro-OMeTAD) was deposited from chlorobenzene with additives at a concentration of 30 mM for lithium bis(trifluoromethanesulfonyl)imide (Li-TFSI) and of 80 mM for *tert*-butylpyridine (*t*BP) *via* spin-coating at 2000 rpm for 45 s. 110 nm thick silver electrodes were thermally evaporated at 1 × 10⁻⁶ mbar through a shadow mask to create solar cells with a total active area of 0.0919 cm², as defined by the overlap between FTO and silver.

Current density-voltage characterization

The current density–voltage (*J*–*V*) curves were measured (2400 Series SourceMeter, Keithley Instruments) in ambient conditions under simulated AM1.5 sunlight at (100 mW cm⁻²) irradiance generated by an Abet Class AAB sun 2000 simulator, with the intensity calibrated with an NREL calibrated KG5 filtered Si reference cell. The mismatch factor was calculated to be less than 1%. The solar cells were masked with a metal aperture to expose a 0.0919 cm² active area for testing of both the current–voltage characteristics and stabilized power conversion efficiency (η_{MPP}). The devices were prebiased at 1.4 V for 5 s before initiating the reverse and forward scans. The scan rate was 0.38 V s⁻¹. Immediately after the *J*–*V* measurements, the η_{MPP} was measured without prebiasing. The devices were kept at the voltage defined at maximum power point, which was determined from the *J*–*V* scans, for 50 s to measure the stabilized power conversion efficiency and current density.

UV-vis-NIR absorption spectroscopy

Absorbance spectra were measured with a Lambda 950 UV-vis-NIR spectrophotometer (PerkinElmer) in a controlled nitrogen atmosphere. The samples were prepared by depositing the respective materials onto solvent-cleaned quartz glass

substrates *via* (co-) evaporation at 10⁻⁷ mbar. A baseline spectrum of clean quartz glass substrate was subtracted from the spectra before further analysis. To analyze the energy region in the optical gap of the ETMs, a background (taking into account Rayleigh scattering and arbitrary linear background) with the form $A = a + bE + cE^4$ was subtracted from the respective spectra; *a*, *b* and *c* are arbitrary fitting parameters, *A* is the absorbance and *E* is the photon energy. Data was smoothed using a 100-point second order Savitzky–Golay filter.

Results and discussion

Vacuum deposition of increasingly thicker layers of 1₂ on FTO leads to a reduction of the electrode WF from 4.6 eV for piranha-cleaned FTO to 3.3 eV when 10 nm of 1₂ are deposited, as shown by UPS spectra in Fig. 2a. The shifts in the secondary electron cut-off (up to 1.2 eV) and in the *E*_F position away from the valence band onset of FTO (up to 0.4 eV) suggest the WF reduction is associated with the formation of an interface dipole at the electrode surface and electron transfer from the dopant to the FTO as seen for other oxides.²⁸ The XPS spectra of dimer-modified FTO (Fig. 2b and Fig. S3 in the ESI†) are consistent with this, showing a Rh^{III} 3d species at 312.1–312.2 eV, which correspond to the monomer cations 1⁺ formed when electrons are donated to the FTO.²⁸ However, XPS reveals most of Rh 3d signal is associated with a Rh^I species at 310.8–310.9 eV, which corresponds to unreacted dimer 1₂ (see ESI† for discussion of the XPS assignment). The ratio between Rh^{III} and Rh^I species slightly increases as more dopant is deposited on FTO, as shown in Table S1.†

To understand how (RhCp**Cp*)₂ affects the energetic alignment at the FTO/ETM interface, vacuum-processible ETMs were used to avoid loss of soluble dopant molecules and/or ions from the substrate during deposition. C₆₀ and PTCBI were evaporated onto piranha-cleaned FTO and on 1₂-covered FTO. UPS shows that upon deposition of the ETMs on the metal-oxide surface the WF decreases from 4.6 eV to 4.4 eV for C₆₀/FTO and to 4.3 eV for PTCBI/FTO, which is attributed to the push-back effect.^{33–35} When FTO is modified with (RhCp**Cp*)₂, the WF of ETM-covered FTO shifts closer to the LUMO of the ETM (Fig. 3). The electron affinity of PTCBI ($EA = E_{\text{vac}} - E_{\text{CB}}$, where *E*_{vac} is the vacuum level) was measured by inverse photoelectron spectroscopy (IPES) to be 4.0 eV (Fig. S1, ESI†), which is similar to that of C₆₀.²³ These changes in WF suggest introducing the interlayer 1₂ between the electrode and the ETM leads to Fermi level pinning of FTO to the LUMO of the ETM. Note that energy-level bending can occur when the metal oxide/ETM interface is strongly Fermi level pinned; in other words the WF of modified FTO/ETM will not exactly align at 4.0 eV.³⁶

Given the high electron affinities of C₆₀ and PTCBI and the effective doping strength of 1₂ (*ca.* -2.0 V *vs.* FeCp₂⁺⁰), from which an effective ionization energy of *ca.* 2.8 eV can be

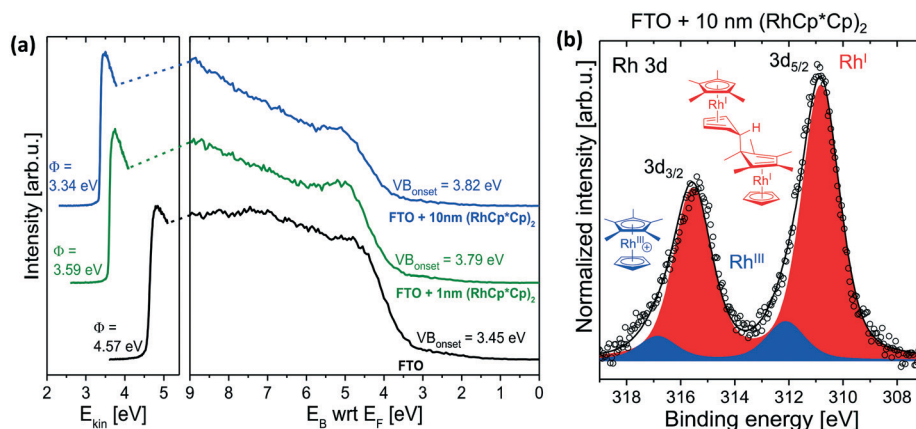


Fig. 2 (a) UPS spectra of piranha-cleaned FTO and of FTO modified with layers of $(\text{RhCp}^*\text{Cp})_2$ (E_{kin} = kinetic energy; E_{B} = binding energy with respect to the Fermi level, E_{F}). (b) XPS spectrum of FTO modified with a 10 nm-thick layer of $(\text{RhCp}^*\text{Cp})_2$ (XPS data for FTO with a 1 nm-thick layer is shown in Fig. S3 in the ESI†).

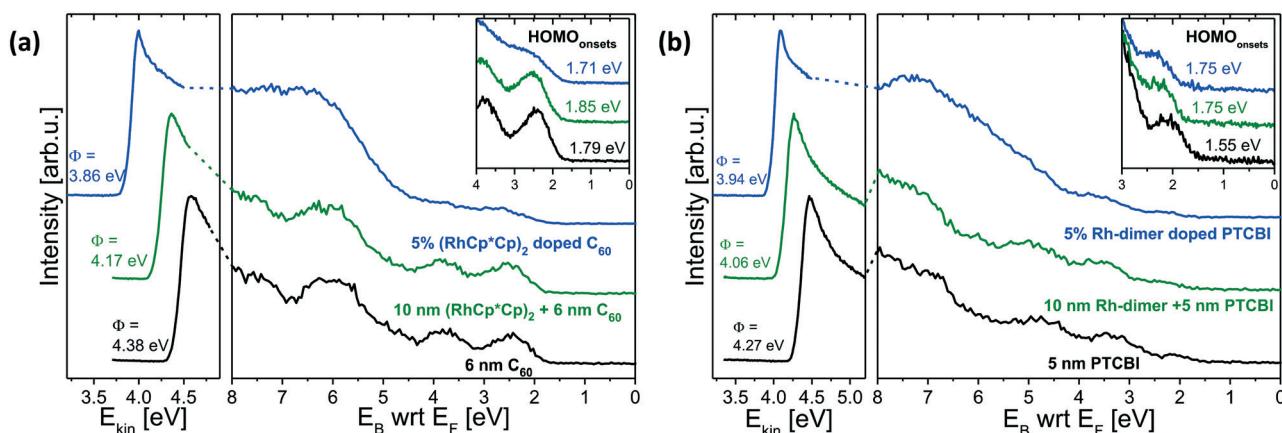


Fig. 3 UPS spectra of FTO/ETM, FTO/10 nm $(\text{RhCp}^*\text{Cp})_2$ /ETM and FTO/doped ETM for (a) ETM = C_{60} and (b) ETM = PTCBI (E_{kin} = kinetic energy; E_{B} = binding energy with respect to the Fermi level, E_{F}). The insets offer enlarged view of the UPS spectra at low binding energies, close to E_{F} . The doping concentration of 5% is given as a molar percentage calculated from the evaporation rates.

estimated),³⁷ it can be expected that upon deposition of these organic semiconductors on the 1_2 -covered electrode surface, the molecules near the interface will be n-doped by unreacted 1_2 through an electron transfer. Additionally, since the WF of the modified FTO is lower than the EA of both ETMs, substrate-to-overlay charge transfer may occur in order to establish a common electron chemical potential.^{38,39}

To show that 1_2 does indeed n-dope these ETMs, we also coevaporated 1_2 with PTCBI or C_{60} (Fig. 3). Compared to modified FTO/ETM samples, coevaporation of $(\text{RhCp}^*\text{Cp})_2$ with the ETM leads to a further reduction of the WF to 3.9 eV and to broadening of the valence band features of both C_{60} and PTCBI, which are typical signatures of doping.^{40,41} XPS spectra confirm that the Rh 3d signal is mostly due to Rh^{III} species (reacted monomer cations, 1^+) when $(\text{RhCp}^*\text{Cp})_2$ is coevaporated with the ETM, and with Rh^{I} species (unreacted dimer 1_2) when the ETM is deposited on 1_2 -modified FTO (see ESI† for discussion of the XPS).

UV-vis-NIR spectroscopy on 1_2 coevaporated with C_{60} shows the presence of an absorption peak at 1065 nm (1.16

eV), which is attributable to $\text{C}_{60}^{\cdot-}$ (Fig. 4, Fig. S7 and S9†).⁴² A similar peak (at ca. 1120 nm, 1.11 eV) is observed when 1_2 is coevaporated with PTCBI, suggesting doping of the perylene derivative. In contrast, the NIR absorption peak is barely observed in the $(\text{RhCp}^*\text{Cp})_2$ -treated FTO/ETM samples, although it becomes more pronounced after sequentially heating the same bilayer at 100, 150, 185 and 200 °C (at least 60 min at each temperature). The appearance of the NIR absorption peak upon annealing corresponds to an increase in formal doping concentration from 0% to 0.6% for C_{60} and 1% for PTCBI, calculated assuming that the dopant molecules are homogeneously dispersed throughout the ETMs. This increase suggests that annealing promotes the reaction of 1_2 with the ETMs, perhaps allowing limited diffusion of the bulky 1^+ into the ETMs.

To assess the ability of PTCBI to act as an ETM for PSCs, and to assess the electrical consequence of introducing an interlayer between the electrode and the two ETMs, n-i-p PSCs were fabricated. The device architecture used was FTO (bare or modified with 10 nm of 1_2)/ETM (C_{60} or PTCBI)/

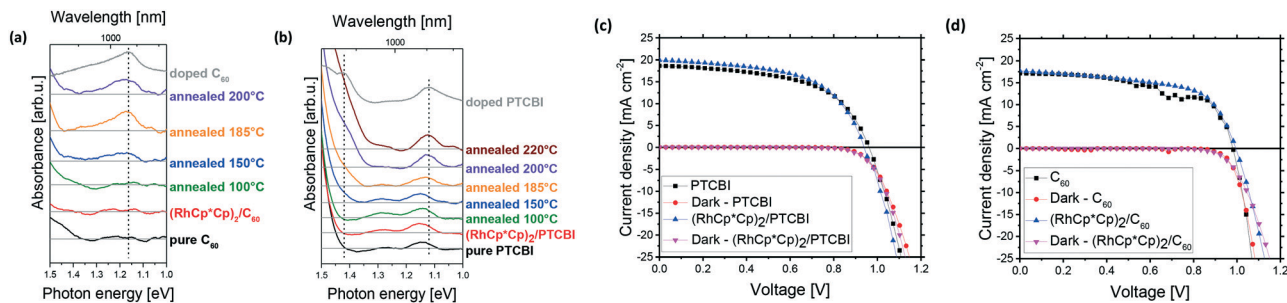


Fig. 4 Smoothed NIR absorption spectra (a and b) for pure ETM, 1_2 -modified FTO/ETM annealed at increasing temperatures, and 1_2 co-evaporated with ETM. The doping concentration for coevaporated ETMs is calculated from the absorption peak at 1065 nm to be 15% for C_{60} (a) and 17% for PTCBI (b). Current density–voltage characteristics for the best performing solar cells fabricated using PTCBI (c) and C_{60} (d) as ETMs before and after deposition of $(RhCp^*Cp)_2$ on FTO.

Table 1 Average device performance parameters of solar cells with evaporated $CH_3NH_3PbI_3$

ETM	J_{sc} ($mA\ cm^{-2}$)	V_{oc} (mV)	FF (%)	PCE (%)	η_{MPP} (%) ^a
C_{60}	17.1 ± 0.3	988 ± 6	55 ± 1	9.3 ± 0.3	9.5 ± 0.4
$Rh(Cp^*Cp)_2/C_{60}$	17.5 ± 0.2	994 ± 5	59 ± 1	10.1 ± 0.3	10.0 ± 0.3
PTCBI	17.4 ± 0.8	928 ± 21	54 ± 1	8.6 ± 0.7	6.8 ± 0.8
$Rh(Cp^*Cp)_2/PTCBI$	19.9 ± 0.2	935 ± 7	56 ± 1	10.4 ± 0.1	9.2 ± 0.1

^a Power conversion efficiency of the devices held at their J - V determined maximum power point for 50 s.

$CH_3NH_3PbI_3$ /spiro-OMeTAD/Ag. Table 1 shows the average device performance parameters, and Fig. 4 shows the current density–voltage (J - V) curves of the champion solar cells with evaporated $CH_3NH_3PbI_3$. Interlayer-free solar cells fabricated using PTCBI as the ETM exhibit similar short circuit current (J_{sc}) and fill factor (FF) but lower open-circuit voltage (V_{oc}) and stabilized power conversion efficiency (η_{MPP}) compared to devices fabricated with C_{60} . However, the deposition of the $(RhCp^*Cp)_2$ interlayer greatly improves the η_{MPP} of devices with PTCBI as ETM from an average of 6.8% to 9.2%. Their J - V determined power conversion efficiency (PCE) also increases from an average of 8.6% to 10.4%. The increase in PCE is a result of both higher J_{sc} and FF, which suggests an improvement in the quality of the FTO/ETM interface upon introduction of $(RhCp^*Cp)_2$. Improvements in PCE and FF are also observed for C_{60} -based solar cells after the electrode/ETM interface is modified using 1_2 . However, changes in η_{MPP} are negligible upon interface modification in C_{60} devices.

We also fabricated cells in which $CH_3NH_3PbI_3$ was processed from a methylamine/acetonitrile precursor solution (as described in the experimental section and in ref. 32). Fig. S10† shows the current density–voltage (J - V) curves for the champion devices with a solution-processed active layer.³² Both C_{60} (ref. 32) and PTCBI (Fig. S6†) are insoluble in methylamine/acetonitrile, preventing the formation of pinholes in the ETM during active-layer deposition. The perovskite absorber processed from solution was annealed for 60 min at 100 °C to ensure its full crystallization. Moreover, annealing promotes more extensive interfacial doping of the ETM in the case of $(RhCp^*Cp)_2$ -modified FTO, as shown by the absorption spectra in Fig. 4 (similar to that seen for other n-doped PDI ETMs²⁰). With optimized processing conditions

stabilized efficiencies up to 12.7% can be obtained using PTCBI as ETM, and up to 14.2% when the FTO/PTCBI interface is modified with 1_2 , as displayed in Table S4.† The fill factor increases more dramatically (from 61% to 67%) with interface modification, when the ETM is doped and brought into ohmic contact with the FTO electrode,⁴³ than in the devices in Table 1; the larger enhancement in FF may be associated with the increased level of interfacial doping of the ETM (Fig. 4) associated with the thermal annealing step used in these devices. However, J_{sc} is somewhat decreased with the 1_2 interlayer.

Conclusions

We have demonstrated that organometallic dimer $(RhCp^*Cp)_2$ can be successfully used to modify the FTO electrode/ETM interface in PSCs, by pinning the Fermi level of the electrode to the LUMO of the ETM and n-doping the molecules of organic semiconductor in proximity of the interface. Vacuum-deposition of $(RhCp^*Cp)_2$ leads to a decrease in the WF of the FTO by more than 1 eV, since the dopant readily transfers electrons to the electrode and forms monomer cations on the metal oxide surface. However, multilayers of unreacted dopant are present, some of which can react with nearby ETM molecules and moderately diffuse after sequential hour-long heating cycles at above 100 °C. This is the first time that the perylene derivative PTCBI is employed as an ETM in a PSC, and n-i-p PSCs fabricated using this organic semiconductor on $(RhCp^*Cp)_2$ -modified FTO lead to some of the highest power conversion efficiencies reported for vacuum-deposited ETMs (up to 14.2%). However, solar cells fabricated using C_{60} under comparable conditions still outperform those

fabricated on PTCBI (16% vs. 12.7%). Nonetheless, the results are consistent with other recent studies^{20–22} in indicating that PDI-type molecules are promising ETMs for PSCs. Specifically, here we show that an vacuum-processible and essentially insoluble derivative can be useful in n-i-p devices; future investigations could explore the potential of other derivatives with these properties.

Conflicts of interest

There are no conflicts to declare.

Acknowledgements

This work was financially supported by the Air Force Office of Scientific Research through project FA9550-15-0115. Work in Berlin was supported by the Sfb951 (DFG) and the Helmholtz Energy-Alliance 'Hybrid Photovoltaics.' M. K. R. acknowledges funding from the European Union's Seventh Framework Programme FP7 (Grant no. 630864). G. M. acknowledges funding from an Oxford-Radcliffe scholarship by University College, Oxford, and from the Engineering and Physical Sciences Research Council (EPSRC) Centre for Doctoral Training in New and Sustainable PV through grant EP/L01551X/1. The authors would like to thank Prof. Gitti L. Frey and Dr David P. McMeekin for helpful discussions.

References

- V. Sivaram, S. D. Stranks and H. J. Snaith, *Sci. Am.*, 2015, **313**, 54–59.
- W. S. Yang, B.-W. Park, E. H. Jung, N. J. Jeon, Y. C. Kim, D. U. Lee, S. S. Shin, J. Seo, E. K. Kim, J. H. Noh and S. I. Seok, *Science*, 2017, **356**, 1376–1379.
- T. Leijtens, G. E. Eperon, S. Pathak, A. Abate, M. M. Lee and H. J. Snaith, *Nat. Commun.*, 2013, **4**, 2885.
- S. K. Pathak, A. Abate, P. Ruckdeschel, B. Roose, K. C. Gödel, Y. Vaynzof, A. Santhala, S. I. Watanabe, D. J. Hollman, N. Noel, A. Sepe, U. Wiesner, R. Friend, H. J. Snaith and U. Steiner, *Adv. Funct. Mater.*, 2014, **24**, 6046–6055.
- K. Wojciechowski, T. Leijtens, S. Siprova, C. Schlueter, M. T. Hörantner, J. T.-W. Wang, C.-Z. Li, A. K. Y. Jen, T.-L. Lee and H. J. Snaith, *J. Phys. Chem. Lett.*, 2015, **6**, 2399–2405.
- S. Jiangjian, X. Xin, L. Dongmei and M. Qingbo, *Small*, 2015, **11**, 2472–2486.
- K. Wojciechowski, I. Ramirez, T. Gorisse, O. Dautel, R. Dasari, N. Sakai, J. M. Hardigree, S. Song, S. Marder, M. Riede, G. Wantz and H. J. Snaith, *ACS Energy Lett.*, 2016, **1**, 648–653.
- D. P. McMeekin, Z. Wang, W. Rehman, F. Pulvirenti, J. B. Patel, N. K. Noel, M. B. Johnston, S. R. Marder, L. M. Herz and H. J. Snaith, *Adv. Mater.*, 2017, **29**, 1607039.
- J. B. Patel, J. Wong-Leung, S. Van Reenen, N. Sakai, J. T. W. Wang, E. S. Parrott, M. Liu, H. J. Snaith, L. M. Herz and M. B. Johnston, *Adv. Electron. Mater.*, 2017, **3**, 1600470.
- Z. Zhu, J. Q. Xu, C. C. Chueh, H. Liu, Z. A. Li, X. Li, H. Chen and A. K. Y. Jen, *Adv. Mater.*, 2016, **28**, 10786–10793.
- C. Sun, Z. Wu, H. L. Yip, H. Zhang, X. F. Jiang, Q. Xue, Z. Hu, Z. Hu, Y. Shen, M. Wang, F. Huang and Y. Cao, *Adv. Energy Mater.*, 2016, **6**, 1501534.
- D. Zhao, Z. Zhu, M. Y. Kuo, C. C. Chueh and A. K. Y. Jen, *Angew. Chem., Int. Ed.*, 2016, **55**, 8999–9003.
- R. Hudej and G. Bratina, *J. Appl. Phys.*, 2003, **93**, 6090–6094.
- H. Zollinger, *Color Chemistry: Syntheses, Properties, and Applications of Organic Dyes and Pigments*, VCH and Wiley-VCH, Zürich and Weinheim, 3rd ed, 2003.
- H. Langhals, *Heterocycles*, 1995, **40**, 477–500.
- L. Calió, C. Momblona, L. Gil-Escrig, S. Kazim, M. Sessolo, Á. Sastre-Santos, H. J. Bolink and S. Ahmad, *Sol. Energy Mater. Sol. Cells*, 2017, **163**, 237–241.
- J. Min, Z.-G. Zhang, Y. Hou, C. O. Ramirez Quiroz, T. Przybilla, C. Bronnbauer, F. Guo, K. Forberich, H. Azimi, T. Ameri, E. Spiecker, Y. Li and C. J. Brabec, *Chem. Mater.*, 2015, **27**, 227–234.
- M. Kaltenbrunner, G. Adam, E. D. Głowacki, M. Drack, R. Schwödiauer, L. Leonat, D. H. Apaydin, H. Groiss, M. C. Scharber, M. S. White, N. S. Sariciftci and S. Bauer, *Nat. Mater.*, 2015, **14**, 1032.
- M. Zhang, T. Li, G. Zheng, L. Li, M. Qin, S. Zhang, H. Zhou and X. Zhan, *Mater. Chem. Front.*, 2017, **1**, 2078–2084.
- S. S. Kim, S. Bae and W. H. Jo, *RSC Adv.*, 2016, **6**, 19923–19927.
- H. Zhang, L. Xue, J. Han, Y. Q. Fu, Y. Shen, Z. Zhang, Y. Li and M. Wang, *J. Mater. Chem. A*, 2016, **4**, 8724–8733.
- J. Huang, Z. Gu, L. Zuo, T. Ye and H. Chen, *Sol. Energy*, 2016, **133**, 331–338.
- S. Olthof, S. Mehraeen, S. K. Mohapatra, S. Barlow, V. Coropceanu, J.-L. Brédas, S. R. Marder and A. Kahn, *Phys. Rev. Lett.*, 2012, **109**, 176601.
- Y. Zhou, C. Fuentes-Hernandez, J. Shim, J. Meyer, A. J. Giordano, H. Li, P. Winget, T. Papadopoulos, H. Cheun, J. Kim, M. Fenoll, A. Dindar, W. Haske, E. Najafabadi, T. M. Khan, H. Sojoudi, S. Barlow, S. Graham, J.-L. Brédas, S. R. Marder, A. Kahn and B. Kippelen, *Science*, 2012, **336**, 327–332.
- L. Lindell, M. Unge, W. Osikowicz, S. Stafström, W. R. Salaneck, X. Crispin and M. P. D. Jong, *Appl. Phys. Lett.*, 2008, **92**, 163302.
- B. Bröker, R.-P. Blum, J. Frisch, A. Vollmer, O. T. Hofmann, R. Rieger, K. Müllen, J. P. Rabe, E. Zojer and N. Koch, *Appl. Phys. Lett.*, 2008, **93**, 243303.
- A. J. Giordano, F. Pulvirenti, T. M. Khan, C. Fuentes-Hernandez, K. Moudgil, J. H. Delcamp, B. Kippelen, S. Barlow and S. R. Marder, *ACS Appl. Mater. Interfaces*, 2015, **7**, 4320–4326.
- K. Akaike, M. V. Nardi, M. Oehzelt, J. Frisch, A. Opitz, C. Christodoulou, G. Ligorio, P. Beyer, M. Timpel, I. Pis, F. Bondino, K. Moudgil, S. Barlow, S. R. Marder and N. Koch, *Adv. Funct. Mater.*, 2016, **26**, 2493–2502.
- S. Guo, S. K. Mohapatra, A. Romanov, T. V. Timofeeva, K. I. Hardcastle, K. Yesudas, C. Risko, J. L. Brédas, S. R. Marder and S. Barlow, *Chem. – Eur. J.*, 2012, **18**, 14760–14772.
- S. R. Forrest, *Chem. Rev.*, 1997, **97**, 1793–1896.

- 31 O. V. Gusev, L. I. Denisovich, M. G. Peterleitner, A. Z. Rubezhov, N. A. Ustynyuk and P. M. Maitlis, *J. Organomet. Chem.*, 1993, **452**, 219–222.
- 32 N. K. Noel, S. N. Habisreutinger, B. Wenger, M. T. Klug, M. T. Horantner, M. B. Johnston, R. J. Nicholas, D. T. Moore and H. J. Snaith, *Energy Environ. Sci.*, 2017, **10**, 145–152.
- 33 H. Vázquez, Y. J. Dappe, J. Ortega and F. Flores, *J. Chem. Phys.*, 2007, **126**, 144703.
- 34 I. Hisao, S. Kiyoshi, I. Eisuke and S. Kazuhiko, *Adv. Mater.*, 1999, **11**, 605–625.
- 35 A. Kahn, N. Koch and W. Gao, *J. Polym. Sci., Part B: Polym. Phys.*, 2003, **41**, 2529–2548.
- 36 M. Oehzelt, N. Koch and G. Heimel, *Nat. Commun.*, 2014, **5**, 4174.
- 37 S. K. Mohapatra, A. Fonari, C. Risko, K. Yesudas, K. Moudgil, J. H. Delcamp, T. V. Timofeeva, J. L. Brédas, S. R. Marder and S. Barlow, *Chem. – Eur. J.*, 2014, **20**, 15385–15394.
- 38 H. Wang, P. Amsalem, G. Heimel, I. Salzmann, N. Koch and M. Oehzelt, *Adv. Mater.*, 2014, **26**, 925–930.
- 39 P. Amsalem, J. Niederhausen, A. Wilke, G. Heimel, R. Schlesinger, S. Winkler, A. Vollmer, J. P. Rabe and N. Koch, *Phys. Rev. B: Condens. Matter Mater. Phys.*, 2013, **87**, 035440.
- 40 B. Lüssem, M. Riede and K. Leo, *Phys. Status Solidi A*, 2013, **210**, 9–43.
- 41 V. I. Arkhipov, P. Heremans, E. V. Emelianova and H. Bässler, *Phys. Rev. B: Condens. Matter Mater. Phys.*, 2005, **71**, 045214.
- 42 F. Li, A. Werner, M. Pfeiffer, K. Leo and X. Liu, *J. Phys. Chem. B*, 2004, **108**, 17076–17082.
- 43 C. Momblona, L. Gil-Escrig, E. Bandiello, E. M. Hutter, M. Sessolo, K. Lederer, J. Blochwitz-Nimoth and H. J. Bolink, *Energy Environ. Sci.*, 2016, **9**, 3456–3463.